Article:

Nakata, T, Phillips, N, Simoes, P et al. (4 more authors) (2020) Aerodynamic imaging by mosquitoes inspires a surface detector for autonomous flying vehicles. Science, 368 (6491). pp. 634-637. ISSN 0036-8075

https://doi.org/10.1126/science.aaz9634

Title:

Aerodynamic imaging by mosquitoes inspires a surface detector for autonomous flying vehicles

Authors: Toshiyuki Nakata[1,2†], Nathan Phillips[1†], Patrício Simões[3], Ian J Russell[3], Jorn A Cheney[1], Simon M Walker[4], Richard J Bomphrey[1*]

Affiliations:

[1]Structure and Motion Laboratory, Royal Veterinary College, Hawkshead Lane, Hatfield, UK, AL9 7TA, United Kingdom.

[2]Graduate School of Engineering, Chiba University, Chiba, 263-8522, Japan.

[3]Pharmacy and Biomolecular Sciences, University of Brighton, Moulsecoomb, Brighton, BN2 4GJ, United Kingdom.

[4]Faculty of Biological Sciences, University of Leeds, Leeds, LS2 9JT, United Kingdom.

*Correspondence to: rbomphrey@rvc.ac.uk

†Contributed equally to this work.

Abstract:

Some flying animals use active sense to perceive and avoid obstacles. Nocturnal mosquitoes exhibit a behavioral response to divert away from surfaces when vision is unavailable, indicating a short-range, mechanosensory collision avoidance mechanism. We suggest this behavior is mediated by perceiving modulations of their self-induced airflow patterns as they enter ground or wall effect. We use computational fluid dynamics simulations of low-altitude and near-wall flights, based on in vivo high-speed kinematic measurements, to quantify changes in the self-generated pressure and velocity cues at the sensitive, mechanosensory, antennae. We validated the principle that encoding aerodynamic information can enable collision avoidance using a quadcopter with a sensory system inspired by the mosquito. Such low power sensing systems have major potential for future, safer, rotorcraft control systems.

One Sentence Summary:

Low power sensing of flow fields by mosquitoes can inspire collision avoidance devices.

Main Text:

At night, in caves, or in otherwise visually compromised environments, animal guidance and control systems must sense and avoid obstacles without relying on optical information.

Mechanoreceptors in arthropods are extraordinarily sensitive and diverse (1), and insects exploit this fully (2), including for the detection of self-induced flows. For example, fields of unidirectional trichoid sensilla are likely to be a key component of the fused sensory input used by flying insects to monitor their attitude (3) and changes in forward speed can be regulated via aerodynamic drag on the antennae (4). In insects, antennal motion is detected by the Johnston's organ (JO) - an array of chordotonal mechanoreceptors located in the antennal pedicel. The JO can detect fluid flows, gravitational pull, and acoustic stimulation and it is one of the most sensitive mechanoreceptive organs in the animal kingdom (5). Mosquitoes, possess exceedingly sensitive JOs. The radial organization of its ~12,000 mechanoreceptive units functionally arranged in antiphase pairs (6), allow mosquitoes to respond to antennal deflections of ±0.0005° induced by ±11 nm air particle displacements in the acoustic near field (Toxorhynchites brevipalpis) (7) or to acoustic particle velocities of ~10^{-7} ms^{-1} (Culex quinquefasciatus) (8).

We take inspiration from such neurophysiological evidence and postulate a sensory mechanism for C. quinquefasciatus that can explain recent behavioral experiments that show mosquitoes avoiding surfaces invisible to their compound eyes (9). The absence of visual cues indicates that another source of close-range information exists, and we hypothesised that these alternative cues are manifest within interactions between the fluid and antennae or hair structures. Specifically, we propose that mosquitoes can detect changes to their self-induced flow patterns caused by the proximal physical environment. These changes to the downwash flow patterns initially generated by the flapping wings arise as the jets of air impinge on the obstacle's surface. This non-contact, sensory modality for flying insects is somewhat akin to the hydrodynamic imaging capability of the lateral line system in fish (10, 11), which is also fundamentally a fluid dynamic, pressure-based system. It would be particularly useful for mosquitoes, which must be adept at stealthy landings on hosts (12) and egg-deposition over water at night.

We demonstrate how nearby surfaces may be detected by mosquitoes by means of the flow field produced during flapping flight (13), which is modulated in response to surfaces at magnitudes sufficient for detection by their mechanosensors. We implement the governing principles onto a miniature, flying vehicle operating close to the ground and walls, fitted with a sensor package that can detect surfaces at distances sufficiently far from collision for effective obstacle avoidance (Movie S1).

Mosquito wingbeat kinematics show high wingbeat frequency, low wingbeat amplitude, and large, rapid span-wise rotations. These features result in unorthodox aerodynamic flows around the wings themselves (13) and two concentrated jets of fast moving air that merge approximately two wing lengths beneath the body. By virtue of the shallow stroke amplitude, the jets are more focused than the wake of other flying animals, which may help to improve the signal if the interaction of the induced flow with a ground plane is important for collision avoidance. Building on our previous data set (13), we performed further CFD simulations at a range of distances from either ground or a wall plane to quantify the effect on local flows around the mosquito (Fig. 1A; S1). Movie S1 shows flow simulations at infinite altitude (where infinite in this case is flight at an altitude far from a surface) and when the jets impinge on a ground plane 10 mm below the mosquito.

Downwash dominates the flow field at higher altitudes. However, at lower altitudes (<10mm), the downwash velocity progressively reduces and recirculation can be seen in some regions, particularly under the body. To see the effect more clearly, we calculated the wingbeat-averaged pressure deltas for each distance relative to the infinite altitude case (Fig.

1C). The zones with the largest pressure deltas are located below the thorax and, surprisingly, above the head. The antennae, with their sensitive JO at the base (7, 8), are therefore well-placed to measure subtle changes in the vector strength of particle velocity in the antero-dorsal region of the head despite being located furthest from the ground. Flow sensitive hairs along the hind leg femur, and elsewhere, could reasonably detect changes in flow velocity associated with these pressure changes too, especially at the lower altitudes, although hind leg hair sensitivity is an order of magnitude lower (Fig. S2). Mosquitoes extend their hind legs towards a surface when landing, and backwards when flying, and are therefore able to compliment the JOs to detect pressure differences due to floor and wall effects. The antennae of flying insects are self-stimulated both by periodic air movements due to wingbeats and by tonic flow due to translation through the air. Recent mosquito tuning data show two sensitivity peaks in male JO. One occurs at lower frequencies (centred at ~280 Hz) and it is tuned to detect the wingbeat frequency of females using an acoustic distortion mechanism (8). A secondary peak of sensitivity is centred on frequencies similar to those at which males fly (600-800 Hz) which would enable a male mosquito to hear its own flight and possibly that of other nearby males (8, 14). Male mosquito JO are therefore adept at perceiving tiny changes in the direction and magnitude of flow velocity of the type associated with proximity to surfaces, potentially using one sensitivity band to detect females and another for detecting changes to their self-generated flow fields when encountering obstacles. In addition to the ground effect, wall surfaces also modulate the simulated flow field (Fig. 1B). Again, changes in pressure distribution can be seen above the head and below the thorax, so both floors and walls could be detected by the same cuticular flow sensors or pressure sensors.

At the male wingbeat frequency, the male JO exhibits a local peak in sensitivity and can detect changes in flow velocities on the order of $10^{-4}\,ms^{-1}$ (Fig. 1D and SI). We include this empirically-derived limit on Figures 1D-F, where we present the change in flow velocity at the wingbeat frequency with varying proximity to the ground (Fig. 1E) and the frequency spectrum of the induced flows (Fig. 1F). Flow velocity oscillates less with altitude, and closer proximity to the ground does not cause oscillations in the flow experienced by the JO to deviate from wingbeat frequency. At higher altitudes, differences in the magnitude of velocity fluctuations at the wingbeat frequency become less pronounced and, for numerical reasons, CFD will eventually fail to capture the very smallest changes in velocity. There is a considerable computational burden as the fine mesh extends to ever more distant ground planes and the velocities deltas tend to zero; nevertheless, a clear trend can be seen whereby the JO can easily detect changes at low altitude but with a diminishing response as the altitude increases until the threshold for detection is not met (Fig. 1E).

The intercept of the CFD-derived velocity changes and the measured sensitivity of the JO predicts a maximum surface detection distance in Culex mosquitoes of 36.4 mm or 20.2 wing lengths. This is a conservative estimate as it only considers the content of the flow signature at wingbeat frequency. Intriguingly, this distance predicted for Culex males is broadly consistent with egg-laying dipping behavior in female Anopheles, where they dip to altitudes of 20-70 mm above the water surface (9). Detection of a ground plane at such distances is far in excess of that which might be expected by the ground effect typically referred to in the aerodynamic literature, where notable improvements in lift and drag force characteristics of wings become negligible beyond an altitude of a single wing length or rotor radius. In our mosquitoes, the negative pressure delta region observed above the head and under the thorax when close to the floor occurs as a result of increasing unsteadiness of the flow in this region, leading to higher peak velocities and lower pressures (Fig. 1C). Conversely, away from surfaces, the flow around the body is relatively steady as the speeds of the wing bases are low.

Mosquitoes are not known to have pressure receptors that could monitor the reflected sound from nearby surfaces in the same manner as echolocating animals. While we do not rule out the possibility that the JO could detect the reflected particle velocity component of self-induced sounds, it would less useful than the pressure component since the particle velocities decrease with the inverse cube of distance rather than the inverse square. Moreover, the frequency of the flight tone means that the wavelength of the acoustic signature is relatively large, on the order of 0.5—1.0m, which limits precision in locating a surface. By contrast, typical echolocation in gleaning bats uses frequencies in the tens of kilohertz, giving a superior resolution by two orders of magnitude. Given the relatively large changes in particle velocity induced by each wingbeat that can comfortably be detected by the JO at altitudes of many body lengths, we offer that this is a more robust solution to surface detection than echolocation.

To show how mechanosensory flow-field monitoring can be used in collision avoidance in autonomous systems, we fitted a small quadcopter platform with a bio-inspired sensor that can that can detect floors and walls using physical principles similar to those described above: specifically, modulation of a deforming flow field. It is lightweight, power-efficient and stealthy, with no additional emission of light or electromagnetic radiation necessary. It is also applicable to rotorcraft or flappercraft of any scale and can work in conditions that are unsuited to alternative range-finding tools. We instrumented an existing 27 g platform (Crazyflie 2.0, Bitcraze, Sweden), with custom circuits and algorithms to identify obstacle proximity based on pressure sensor readings. The stand-alone sensor module performs reliable obstacle detection up to three rotor diameters away during autonomous flights.

The device, like the mosquito, will be most sensitive if sensors are mounted at locations experiencing the greatest changes in the flow field when approaching surfaces. Nearby surfaces distort the flow field all around the body – making surface detection simple, direct and robust – but, to determine optimal sensor design, number and placement, it is necessary to find the most affected regions. We used stereo particle image velocimetry to measure fluid velocities around the quadcopter at various altitudes and proximities to a wall (Fig. 2; S3). These flow measurements were used to inform the position of probe tubes relative to the annular jets and regions of recirculation under the control boards. The probes were connected to differential pressure sensors, which are a more accessible solution than particle-velocity probes (Fig. 3; S4-7). Since the dynamic pressure is proportional to the square of flow velocity the same physical phenomenon underpins the sensing capability. Ground effect could be detected using a pair of probes extending above and below the craft, while the direction of nearby walls could be detected by using paired probes extending fore-aft, laterally, or diagonally. Further detail on the design criteria and the pressure delta thresholds for each proximity condition are detailed in Supplementary Material.

This simple model could detect both ground and wall effects. Pressure differential increases with surface proximity (Fig. 3F-G) and of sufficient signal to provide alarm thresholds (Table S1,S3) for each proximity condition. The complete module weighed just 9.2g (see Table S2 for detailed mass breakdown).

The device successfully emulated the mosquito model behavior by identifying nearby obstacles during flight. Initially the quadcopter was flown tethered (Fig. 4A-B), then piloted (Fig. 4C) and, finally, autonomously using positional feedback from a motion capture system. Ground (Fig. 4D; S9-10) and wall planes (Fig. 4E-G) could be discriminated using appropriately placed sensor combinations monitoring induced flow field changes. Previous quadcopter studies have detected proximal surfaces by combining measured rotor speeds required for stable hovering with an aerodynamic model of the rotor and the motor speed required to support weight (15). Others have detected external flows such as fans emulating the downwash of another vehicle (16) or successfully incorporated flight dynamics models of the specific quadcopter platform and used them to infer obstacle proximity by the forces and torques acting on the vehicle (17). Our method requires no a priori aerodynamic or rigid body models to function, but rather requires only basic thresholds. It is therefore a more direct measure of surface proximity and needs little or no processing to function.

References

1. F. G. Barth, A Spider's World: Senses and Behavior. (Springer, Berlin, 2002).
2. M. C. Göpfert, R. M. Hennig, Hearing in Insects. Annu. Rev. Entomol. **61**, 257-276 (2016).
3. G. K. Taylor, H. G. Krapp, in Advances in Insect Physiology: Insect Mechanics and Control. (2008), vol. 34, pp. 231-316.
4. T. Roy Khurana, S. P. Sane, Airflow and optic flow mediate antennal positioning in flying honeybees. eLife **5**, e14449 (2016).5. L. H. Field, T. Matheson, in Adv. Insect Physiol., P. D. Evans, Ed. (Academic Press, 1998), **27**, pp. 1-228.
6. D. N. Lapshin, D. D. Vorontsoy, Directional and frequency characteristics of auditory neurons in Culex male mosquitoes. J. Exp. Biol. **222**, jeb208785 (2019).
7. M. C. Göpfert, H. Briegel, D. Robert, Mosquito hearing: sound-induced antennal vibrations in male and female Aedes aegyptii. J. Exp. Biol. **202**, 2727-2738 (1999).
8. P. M. V. Simões, R. A. Ingham, G. Gibson, I. J. Russell, A role for acoustic distortion in novel rapid frequency modulation behavior in free-flying male mosquitoes. J. Exp. Biol. **219**, 2039-2047 (2016).
9. F. Hawkes, G. Gibson, Seeing is believing: the nocturnal malarial mosquito Anopheles coluzzii responds to visual host-cues when odour indicates a host is nearby. Parasites & Vectors **9**, 320 (2016).
10. S. Dijkgraaf, The functioning and significance of the lateral-line organs. Biol. Rev. **38**, 51-105 (1963).
11. M. Yoshizawa, W. R. Jeffery, S. M. van Netten, M. J. McHenry, The sensitivity of lateral line receptors and their role in the behavior of Mexican blind cavefish (Astyanax mexicanus). J. Exp. Biol. **217**, 886-895 (2014).

12. F. T. Muijres et al., Escaping blood-fed malaria mosquitoes minimize tactile detection without compromising on take-off speed. J. Exp. Biol. **220**, 3751-3762 (2017).

13. R. J. Bomphrey, T. Nakata, N. Phillips, S. M. Walker, Smart wing rotation and trailing-edge vortices enable high frequency mosquito flight. Nature **544**, 92-95 (2017).

14. D. N. Lapshin, Mosquito bioacoustics: auditory processing in Culex pipiens pipiens L. males (Diptera, Culicidae) during flight simulation. Entomol. Rev. **92**, 605-621 (2012).

15. C. Powers, D. Mellinger, A. Kushleyev, B. Kothmann, V. Kumar, in Experimental Robotics: The 13th International Symposium on Experimental Robotics, J. P. Desai, G. Dudek, O. Khatib, V. Kumar, Eds. (Springer International Publishing, Heidelberg, 2013), 289-302.

16. D. W. Yeo, N. Sydney, D. A. Paley, D. Sofge, Downwash detection and avoidance with small quadrotor helicopters. **40**, 692-701 J. Guidance, Control and Dynamics. (2016).

17. C. D. McKinnon, A. P. Schoellig, Estimating and reacting to forces and torques resulting from common aerodynamic disturbances acting on quadrotors. Robot. Auton. Syst. 103314 (2019).

18. H. Liu, Integrated modeling of insect flight: from morphology, kinematics to aerodynamics. J. Comput. Phys. **228**, 439-459 (2009).

19. S. M. Walker, A. L. R. Thomas, G. K. Taylor, Operation of the alula as an indicator of gear change in hoverflies. J. R. Soc. Interface, **9**, 1194-1207 (2011).

Supplementary Materials only:

20. T. Nakata, H. Liu, Aerodynamic performance of a hovering hawkmoth with flexible wings: a computational approach. Proc. R. Soc. B **279**, 722-731 (2012).

21. M. C. Göpfert, D. Robert, Active auditory mechanics in mosquitoes. Proc. Biol. Sci. **268**, 333-339 (2001).

22. B. Warren, A. N. Lukashkin, I. J. Russell, The dynein-tubulin motor powers active oscillations and amplification in the hearing organ of the mosquito. Proc. R. Soc. B **277**, 1761-1769 (2010).

Acknowledgements:

The authors are grateful for discussions with the RVC flight group, P. Kimber and C. Jones of Dstl and N. Short. We thank Professor H. Liu of Chiba University for permission to use the CFD simulator. **Funding:** This work was funded, in part, by the Autonomous Systems Underpinning Research (ASUR) programme under the auspices of the Defence Science and Technology Laboratory (Dstl), UK Ministry of Defence and, in part, by the Biotechnology and Biological Sciences Research Council (BB/J001244/1), both to RJB. SMW was supported by a Royal Society University Research Fellowship. Work at the University of Brighton was funded by the Medical Research Council (MR/ N004299/1). PS was partly supported by the Rising Stars award from the University of Brighton. **Author contributions:** RJB conceived the experiments with TN, NP, SMW and IJR. SMW, IJR and PS advised on experimental protocol. NP designed and built the quadcopter sensor module. NP and JC built quadcopter module communication links. IJR and PS gathered and processed data for the JO and femoral hairs. RJB, TN, NP and SMW wrote the manuscript. All authors contributed to editing the manuscript.

Competing interests: Some of this work was used to support, in part, patent filing WO 2019/002892 A1. **Data and materials availability:** All data is available in the main text or the supplementary materials. Mosquito kinematics are available via (13). The CFD solver (18) and kinematics acquisition code (19) are described in further detail elsewhere.

Fig. 1. Velocity and pressure distributions around mosquitoes flying near surfaces. A) Front view of a mosquito hovering at five altitudes measured from the mosquito body with downwash shown in blue and the upwash in red. Flow visualisation plane at maximum wingspan. A discrete jet from each wing merges in the infinite and high altitude cases. B,C) Side view of a hovering mosquito (grey), and distribution of absolute wingbeat-averaged mean difference in pressure relative to the infinite case $\overline{|\Delta P|}$ (Pa), measuring in the sagittal plane. The pressure distribution in free airspace is compared to flight B) near a wall (where the wall is the left edge of the panel), and C) at varying altitudes; white cross shows monitoring location corresponding to the tip of the antenna. D) The particle velocity detection threshold of the male JO shows a secondary notch of enhanced sensitivity (white arrow) within the male wingbeat frequency range (see supplementary material for electrophysiology methods and also (8)). Grey shading indicates the range of male wingbeat frequencies observed during free flight. The JO's secondary notch has a particle velocity sensitivity shown by the solid line. The primary notch at approximately 200 Hz is used for mating communication and is tuned to tones generated by the male-female wingbeat frequencies' distortion product. E) The amplitude of change in velocity magnitude at wingbeat frequency measured at the antennae increases with proximity to the ground. A straight line of best fit is plotted (blue, with dashed 95% confidence intervals) to show the intersection with the JO flow velocity sensitivity at the male wingbeat frequency alone (solid horizontal line). F) The amplitude of changes in velocity magnitude at the antennae in the frequency domain, calculated as the Fast Fourier Transform at infinite altitude subtracted from the FFT at a given altitude over 50 wingbeat cycles. Differences are always greatest at wingbeat frequency, irrespective of altitude. Asterisk shows JO particle velocity sensitivity at wingbeat frequency.

Fig. 2. Quadcopter flow field characterisation. A) Slices showing induced downwash for a quadcopter hovering at a range of altitudes in multiples of rotor diameter (D = 46mm). Line integral convolution shows instantaneous streamlines and color flood shows vertical velocity. B) Difference in velocity magnitude at altitude range of altitudes. C) Schematic of the craft showing the PIV measurement plane (red) with respect to a centreline (dashed). D) Oblique and E) Top view of the three-dimensional flow field at altitude of 2D. Four annular jets emanate from the rotors and recirculate under the fuselage (iso-surface of downwash and upwash: 4 ms^{-1} in red; -2 ms^{-1} in blue). Outline of the quadcopter in green, for reference.

Fig. 3. Bio-inspired sensor module. A) arrangement and placement of five paired pressure probes placed to maximise pressure deltas when close to surfaces; B) pressure sensor module components comprising the pressure sensor array, adapter PCB and microcontroller; C) schematic showing internal routing tracks connecting paired probes [Fore-Aft in green, Port-Starboard in yellow, ForwardPort-AftStarboard in dark blue, ForwardStarboard-AftPort in orange, Top-Bottom in light blue] to pressure sensors via a tube network shown in D); E) free flying prototype with mosquito-inspired surface detection device; F,G) Differential pressure delta with proximity to ground (F) and wall (G); shaded regions indicate one standard deviation. Altitude is measured from the plane of the rotor hubs. Wall proximity is measured from the nearest rotor hub.

Fig. 4. Demonstration of aerodynamic imaging in a quadcopter. A) tethered wall proximity test with wall on forward side of quadcopter. Yellow triangles point at forward and aft red indicator lights; B) tethered ground proximity test. Yellow arrows show all four red alarm lights illuminating when ground is detected; C) piloted free flight test of ground detection; D) long exposure photographs of autonomous test of ground detection. Oblique side view showing perpetual flight lights in blue, detection indicator lights in red. The ground was detected twice; E-G) top view of three wall detection trials. A single surface detection indicator light illuminates on one side nearest the wall before the quadcopter moves away from the obstruction. A strobe flash prior to the end of the exposure captures the quadcopter towards the end of its flight.

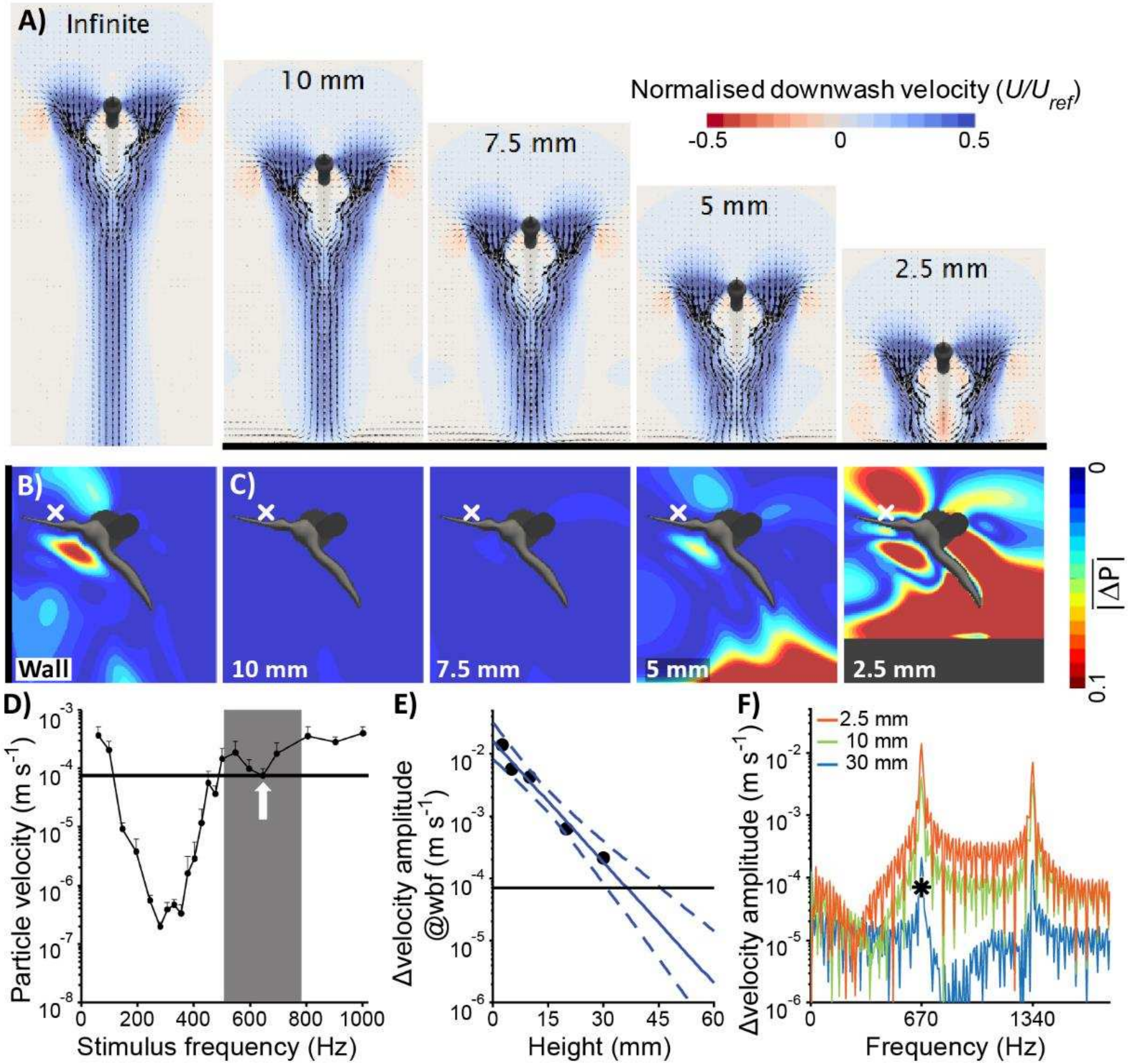

A) Infinite
10 mm
7.5 mm
5 mm
2.5 mm
Normalised downwash velocity (U/U_{ref})
-0.5
0
0.5
B)
C)
Wall
10 mm
7.5 mm
5 mm
2.5 mm
0
$\overline{|\Delta P|}$
0.1
D)
Particle velocity ($m\ s^{-1}$)
Stimulus frequency (Hz)
E)
Δvelocity amplitude @wbf ($m\ s^{-1}$)
Height (mm)
F)
2.5 mm
10 mm
30 mm
Δvelocity amplitude ($m\ s^{-1}$)
Frequency (Hz)
670
1340

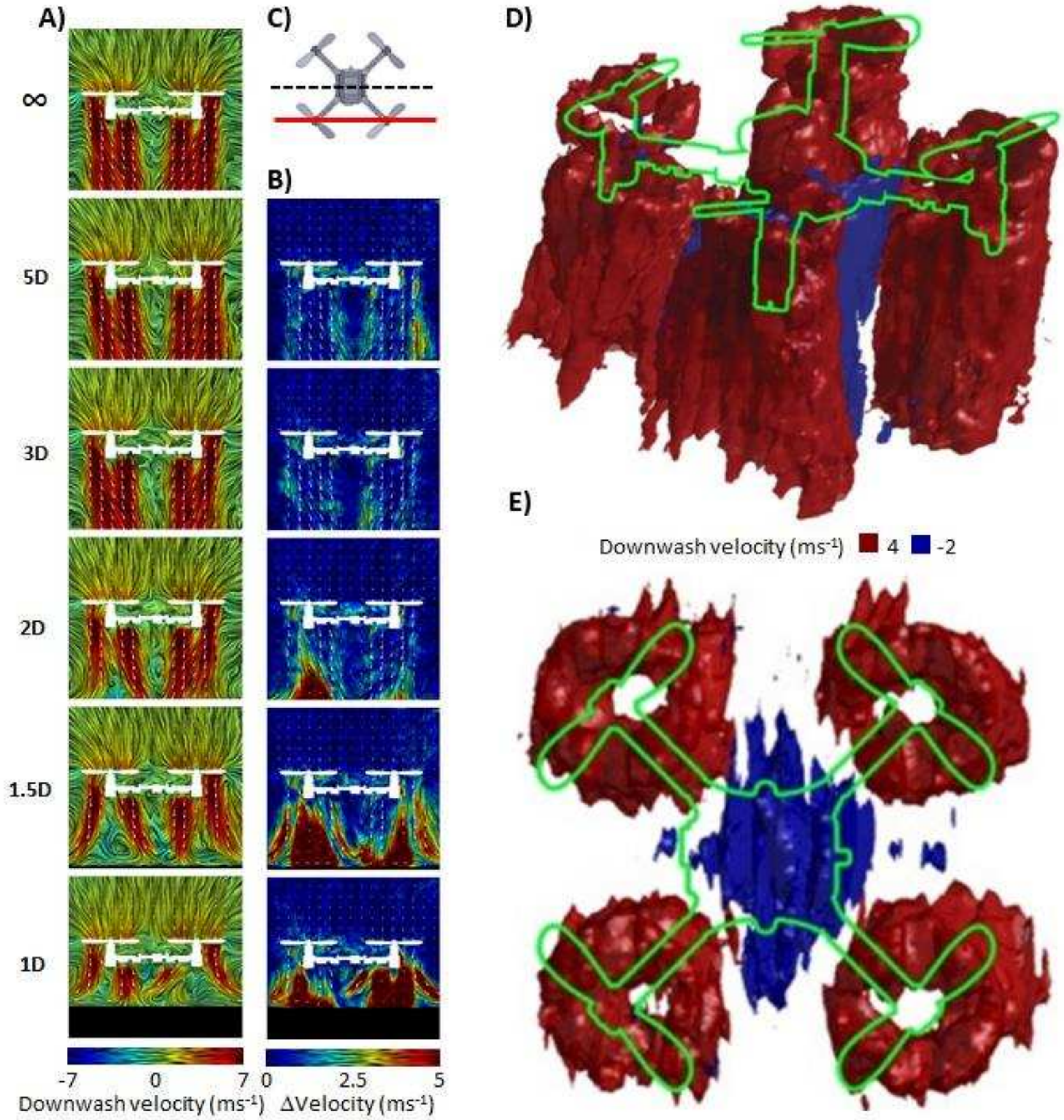
A)
C)
D)
B)
E)
∞
5D
3D
2D
1.5D
1D
-7
0
7
Downwash velocity (ms-1)
0
2.5
5
ΔVelocity (ms-1)
Downwash velocity (ms-1)
4
-2

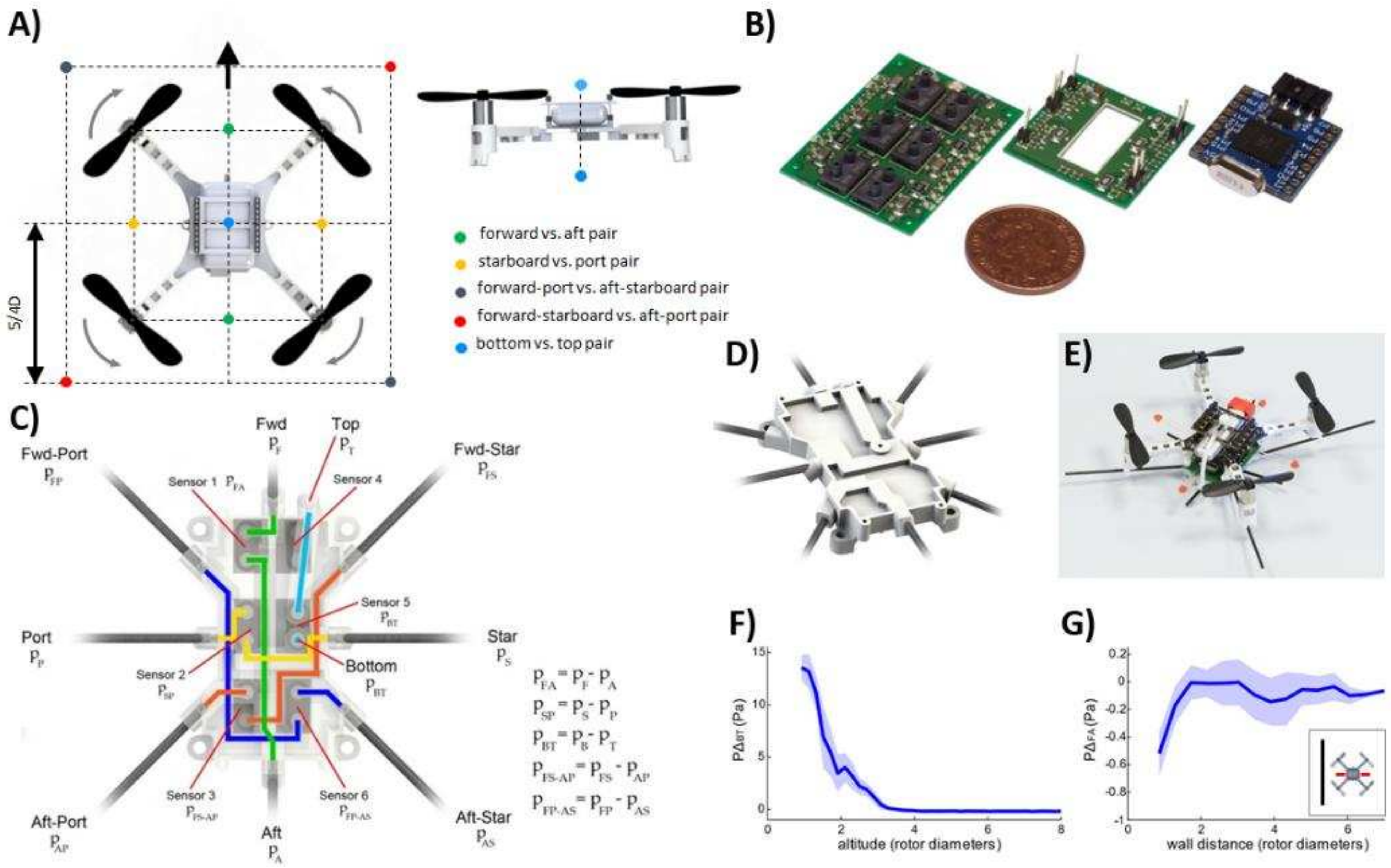

A)
B)
C)
D)
E)
F)
G)
5/4D
forward vs. aft pair
starboard vs. port pair
forward-port vs. aft-starboard pair
forward-starboard vs. aft-port pair
bottom vs. top pair
Fwd
Top
Fwd-Port
Fwd-Star
Sensor 1
Sensor 4
Sensor 5
Port
Star
Sensor 2
Bottom
Sensor 3
Sensor 6
Aft-Port
Aft
Aft-Star
$P_{FA} = P_F - P_A$
$P_{SP} = P_S - P_P$
$P_{BT} = P_B - P_T$
$P_{FS-AP} = P_{FS} - P_{AP}$
$P_{FP-AS} = P_{FP} - P_{AS}$
PΔBT (Pa)
altitude (rotor diameters)
PΔFA (Pa)
wall distance (rotor diameters)

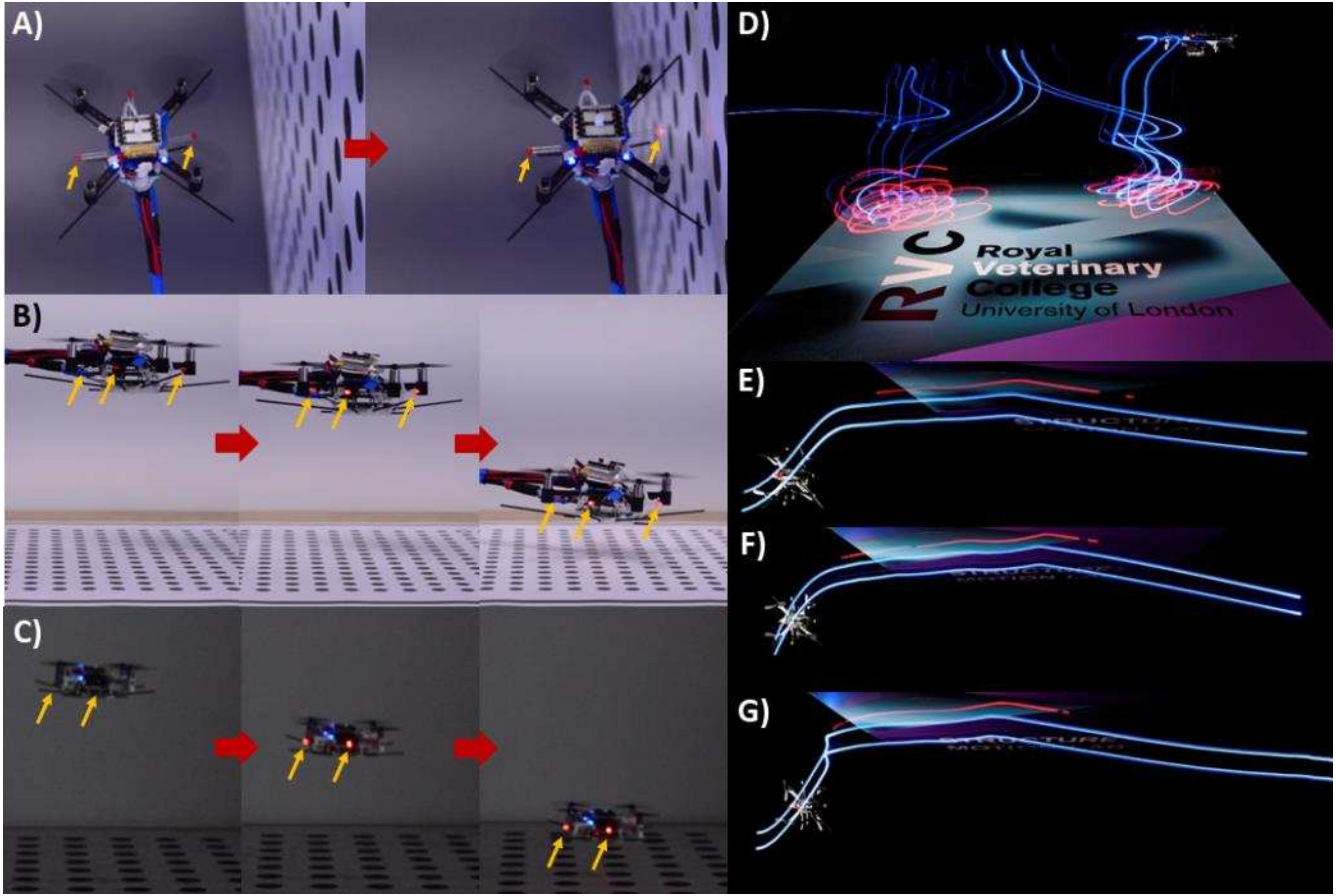
A)
B)
C)
D)
Royal
Veterinary
College
University of London
E)
F)
G)

Supplementary Materials for

Aerodynamic imaging by mosquitoes inspires a surface detector for autonomous flying vehicles

Toshiyuki Nakata[1,2†], Nathan Phillips[1†], Patrício Simões[3], Ian Russell[3], Jorn A Cheney[1], Simon M Walker[4], Richard J Bomphrey[1*]

Correspondence to: rbomphrey@rvc.ac.uk

This PDF file includes:

Materials and Methods
Figs. S1 to S10
Tables S1 to S3
Captions for Movie S1

Other Supplementary Materials for this manuscript include the following:

Movie S1

Materials and Methods

Computational Fluid Dynamics

For our CFD model, we used a dynamic flight simulator based on the incompressible, unsteady, three-dimensional Navier-Stokes equations (13, 18, 20). Implementation of the CFD solver is outlined and validated for insect-scale fluid dynamics in (18). By using a validated CFD solver, our results should be solver agonistic and similarly validated solvers should produce comparable results. The simulator utilizes a multi-block, overset-grid method in which the computational domain is decomposed into the local grid, clustered in the vicinity of the wings and body, and a global Cartesian grid. The wing and body grids were generated from a surface mesh acquired using a voxel carving technique (19). The minimum grid spacing from the surface is based on 0.1/sqrt(Re), where Re is the Reynolds number. The distance between the surface and outer boundary was set to be 2.0 c_m (mean chord lengths) for the wings and 1.0 c_m for the body grids. The outer boundary conditions for local grids are given by a Cartesian background grid (28R × 14R × 28R). We assumed a symmetric motion of the left and right wings, and applied a symmetric boundary condition at the sagittal plane of the body and background grids. The wing grid regenerated every time-step after the wing surface twisted and rotated around the hinge. Flapping angles were interpolated by a fifth order Fourier series.

Sequences other than those at infinite altitude required a fine mesh (0.02 c_m) extending to the ground plane. This gave sufficient resolution in computing the complex flow interactions in these regions with the consequence of substantially increased simulation time. Flow fields were computed for several flight altitudes of: infinite altitude, 5.4 (30 mm), 3.6 (20 mm), 1.8

(10 mm), 1.35 (7.5 mm), 0.9 (5 mm) and 0.45 (2.5 mm) wing lengths from the ground. Standardised wing kinematics were used for all simulations, selected by identifying the mean kinematics of the individual with kinematics closest to the mean of all individuals measured. The kinematics and detailed description of their acquisition are available in (13).

Convergence of the flow field calculations to a steady periodic result

For the simulation to converge on a steady solution, it was necessary to calculate a sufficient number of wingbeats such that the flow could convect to the ground plane, interact with the surface, and subsequently propagate back up to the mosquito. Unsurprisingly, this duration varied with altitude and, again, processing time increased greatly with distance on account of the larger volume of fine resolution mesh. Our convergence metric was the difference in mean flow velocity (in comparison with the infinite altitude case) at a location in the simulated flow field corresponding to the tip of one antenna (Fig. S1).

Sensitivity data

*Johnston'*s Organs (JO)

Male Culex quinquefasciatus mosquitoes (N=6) were immobilized by cold narcosis and fixed with beeswax to a 5mm side brass block. The pedicel, head and legs were immobilized using superglue. Acoustic stimuli were delivered to the preparation from a modified DT48 headphone speaker, coupled to a 7mm (internal diameter) plastic tube. The point of the tube was positioned at the level of the mosquito head and at 10 mm from the tested antennae (8).

Compound extracellular receptor potentials were measured from the JO with tungsten electrodes (5–7MΩ, 1 μm tip, part no. WE30032.OH3, MicroProbes, Gaithersburg, MD, USA) that were advanced with a Märzhäuser PM10 (GmbH) manipulator so that the tip of the electrode just penetrated the wall of the pedicel. In this location, voltage responses from the JO are dominated by compound, phasic receptor potentials from the scolopidia that are twice the frequency of the acoustic stimulus. All measurements were made on a vibration-damped table (model: M-VW-3036-OPT-99-9-28-92, Newport Corporation) inside an IAC sound-attenuated booth.

Signals from the electrodes were amplified (10,000-fold) and low-pass filtered (5 kHz) using a custom-built differential pre-amplifier. Pure tones of 82 ms duration with 8 ms rise/fall time were delivered via a 5 kHz low-pass filter and calibrated against a known 94 dB sound pressure level (21) using a Bruel & Kjaer 4230 microphone. Voltage signals for the sound system were generated and voltage signals from the electrodes were digitized at 250 kHz via a Data Translation 3010 D/A A/D card using programs written in Matlab. Raw data and online computation of the magnitude and phase of the phasic voltage signals were stored in ASCII files for display and further analysis. All recordings were made within 30 min of preparation to ensure optimal physiological state and hearing sensitivity. Temperature control for the experiments was provided by placing the mosquito preparation in a chamber machined in a Peltier-controlled heat sink (22). Current was fed to the Peltier element by a power supply with a negative feedback control from a thermistor (80TK, Fluke) which was thermally coupled to the chamber.

We recorded and measured the magnitude of the fundamental frequency component of the extracellular electrical responses from the JO as a function of stimulus level (particle velocity) to pure sinusoidal tones between 61 and 1001 Hz. The threshold sensitivity for each stimuli frequency was obtained by determining the particle velocity threshold at which the electrical signal elicited a response 5 dB above the noise floor of the recording.

Femoral trichoid sensilla

We used a similar method to measure the velocity response characteristics of femoral hair flow sensors at a range of frequencies for five male C. quinquefasciatus mosquitoes. The sensitivity peaks at lower frequencies than those of the JO and they are less sensitive overall (Fig. S2). They are an order of magnitude less sensitive once the frequency exceeds 120Hz, and relatively insensitive above 300Hz, indicating they are more receptive to a low frequency, or even DC component of the recirculating flow.

<u>Quadrotor flow fields</u>

We measured detailed flow fields produced by the Crazyflie 2.0 quadcopter at a range of floor and wall proximities using stereo particle image velocimetry (stereo-PIV). The experimental setup is illustrated in Figure S3, where a pair of stereo 1024 x 1024px high-speed cameras (Photron SA3, Photron Europe, Ltd) captured seeding particles in a ~1mm thick light sheet. Illumination was provided by a 527nm 1kHz Nd:YLF laser (Litron LDY-300PIV, Litron Lasers, Ltd. UK) with the beam passing through light sheet optics to focus the beam and diverge in a single axis. A spherical mirror was used to reflect the laser light sheet back within the same plane to illuminate shadowed areas cast by the quadcopter, thus giving comprehensive illumination around the craft.

Seeding droplets of olive oil (~1µm) were emitted by an aerosol generator and allowed to become quiescent in a large tented enclosure that contained the particles. The two cameras were fitted with 105mm lenses (AF Nikkor, f2.8) with one camera aligned normal to the light sheet, and the second camera viewing at approximately 45° angle from normal, requiring a Scheimpflug lens mount to maintain focus across the measurement plane.

A Perspex sheet (1 × 1 m) stiffened with an aluminium angle frame served as a floor or wall surface. For wall tests, we simply rotated the quadcopter 90° from its typical horizontal attitude. The height of the surface could be adjusted to set the floor / wall distance from the quadcopter. The reflective surface of this boundary, and its transparency, minimized scattered glare. This procedure allowed flow field measurements to be recorded successfully very close to the surface: within approximately 1 mm.

The quadcopter was mounted at its aft end to a sting connected to a traverse, which enabled translation in 2 mm increments relative to the measurement plane. Thus, the entire volume (of 85 measurement planes) around the quadcopter could be measured, resulting in a dense 3D grid of three-component flow velocity vectors. A microcontroller traversed the quadcopter at set distance and time intervals, and also triggered the stereo-PIV measurement via a high-speed controller. Flow field measurements for a given floor or wall distance configuration were completely automated and repeatable.

During flow characterisation measurements, the quadcopter motors were powered by an external power supply and driven at a frequency of 230 Hz, which corresponded to a thrust equivalent to the quadcopter weight far from the ground. At each flow field measurement location across the craft, 12 stereo-PIV measurements were captured at a frequency of 250 Hz. This rate avoided phase-locking of the rotor blades and gave unbiased time-averaged velocity values. The measurement area was calibrated with a dual-plane 105 × 105 mm calibration plate. This enabled the raw image pairs to be processed into three-component vector maps using DaVis 8.0.8 (LaVision UK Ltd, Oxfordshire). For processing, a stereo cross-correlation algorithm was used with an initial interrogation window size of 32 × 32 px progressing to a final window size of 16 × 16 px with a 50% overlap and deformable windows. Between passes, a median filter was used to identify and remove spurious vectors, where vector components of twice the RMS value of their neighbouring components were considered outliers. After processing, any regions with empty spaces were filled via interpolation. Finally, the 12 vector maps for each of the 85 planes across the craft were ensemble-averaged and arranged into a 3D volume.

Sensor module design

The key element of the pressure sensor module is the pressure sensor array for monitoring the near pressure field. We designed a custom PCB fitted with six digital differential pressure sensors (model SDP31 Sensirion Inc.) with a measurement range of ±500 Pa, 16 bit resolution, and a mass of 0.2 g each (Fig. S2).

A pressure probe routing component was designed and fabricated with internal tracks maintaining a fluid connection to their corresponding differential pressure sensors (Fig. S5). This component allowed the probes to be positioned in regions of high velocity deltas for improved surface detection signal-to-noise. Routes and connections are shown in Figure S5b, where the probe locations are labelled along with their symbol ‘p_i’ denoting the pressure at the i^{th} probe location. For a given sensor measuring the differential pressure of probe ‘i’ relative to probe ‘j’, the resulting pressure reading p_{ij} for that sensor is computed as $p_{ij} = p_i - p_j$. These definitions are given for each of the sensors in Figure S5b. Only five of the six available sensors were used.

The probe attachment component was manufactured by selective laser sintering 3D printing of nylon in two halves, as shown in Fig. S6A. The halves were bonded together using epoxy with a layer of Tyvek between (Fig. S6A, right) to close off the channels and to provide channel routing between the layers through holes in the relevant areas. Tyvek was used because it is light weight and stretch resistant. Pressure probes were made from carbon fibre tube with 1.5 mm outer diameter and 0.7 mm internal diameter. The probe assembly ready for connection is illustrated in Fig. S6B.

We used a Propeller Mini microcontroller (Parallax Inc.) for receiving and processing the pressure sensor values (Fig. S7). It was modified from its original form by removing the portion of a board with a set of higher voltage regulators. This reduced the board size by more than half, as well as significantly reducing its mass. The microcontroller features a parallel architecture with eight separate cores that allow for parallel processing at a clock speed of 80 MHz. It was programmed to read pressure values (via I^2C) from each of the six sensors at a rate of 1 kHz, and perform moving average and RMS computations on the readings. Algorithms monitored whether each channels surpassed pre-set thresholds corresponding to a floor or wall proximity condition.

To fit the sensor module to the quadcopter and allow it to receive on-board power, a second PCB was designed to adapt the connections to that of the Crazyflie (Fig. S7). This adapter board connects the microcontroller to the quadcopter I^2C input bus, and was also fitted with forward, back, and side-facing LEDs to provide a visual indication of the proximity condition as determined from the processed pressure sensor values. These individual components were designed to be modular, simply stacking on top of each other when fitted to the Crazyflie 2.0 underside (Fig. S8).

System architecture

The system architecture comprising the quadcopter, a pressure sensor array, connecting elements, guidance, navigation and control is shown in Figure S9. This consists primarily of the Crazyflie quadcopter platform, which is tracked in 3D space by an array of motion capture cameras that feed this positional data via UDP communication to a PC-based flight outer loop controller. The controller receives telemetry and commands the quadcopter to update its position via radio link.

The array of pressure sensors fitted around the quadcopter communicate via I^2C to a dedicated microcontroller, which serves the sole function of receiving and filtering the pressure values. It then processes the pressure data streams to determine if a floor or wall is within close proximity, and – if so – in which direction it lies. The determination is based on pre-programmed pressure thresholds determined during tethered trials. A more sophisticated algorithm would characterise change in the pressure distribution as a function of throttle. If scaled to alternative platforms, the thresholds required are likely to be different from those we use here. However, since the mechanism is based on downwash and recirculation, there is no physical impediment for this type of surface detection working at all scales of rotorcraft and flappercraft, so long as suitable thresholds are selected.

The microcontroller sends a ‘proximity condition’ to the quadcopter’s microcontroller. Here, the proximity condition simply takes the form of an integer which has the representations listed in Table S1. The quadcopter then displays the proximity condition by illuminating, or otherwise, the four onboard display LEDs. It can also relay this proximity condition along with its standard telemetry parameters (attitude, battery level, etc.) to the PC-based flight controller.

Size, weight and power

The mass breakdown for the pressure sensor module along with the power consumption values are summarised in Table S2. The original quadcopter battery (240 mAh LiPo), was replaced with a battery of 38% lower mass (with 150 mAh capacity) as this improved the flight time when carrying the added payload of the pressure sensor module. With the exception of the protruding proximity condition indicator LEDs and pressure probes, the pressure sensor module measures 39 × 27 × 14 mm.

Pressure differential delta thresholds

From preliminary tethered flight tests, pressure thresholds were selected that correspond to a known floor or wall proximity conditions. A threshold of 0.5 Pa was chosen for a floor proximity condition, and 0.3Pa was selected for a wall forward / aft condition. The different combinations of bottom versus top pressure differential ($P\Delta_{BT}$) and forward versus aft differential ($P\Delta_{FA}$) values that correspond to the proximity conditions are summarised in Table S3. If the $P\Delta_{BT}$ and $P\Delta_{FA}$ values meet both conditions for a given row, then the pressure sensor module has identified that the corresponding proximity condition has occurred. Algorithms were programmed into the pressure sensor module to identify proximity conditions from the listed pressure differential combinations. Starboard and port wall conditions have been excluded because wall detection in this direction is much less sensitive due to counter rotation of adjacent rotors. Fortunately, however, quadcopters can fly in any orientation so this is of little practical consequence.

<u>Autonomous flight arena</u>

A schematic of the autonomous flight arena for providing closed-loop control of the quadcopter trajectory is shown in Fig. S10. As is becoming commonplace, the quadcopter was fitted with retroreflective markers tracked by 12 motion capture cameras (Qualisys; 100 Hz) which provide marker coordinates in the calibrated lab space to a central computer. The computer runs an outer loop flight controller with the Linux Robot Operating System (ROS) that accepts the marker positions, computes the quadcopter position and orientation, and then transmits commands to the quadcopter to update its according to the set point error calculated in its current position and orientation.

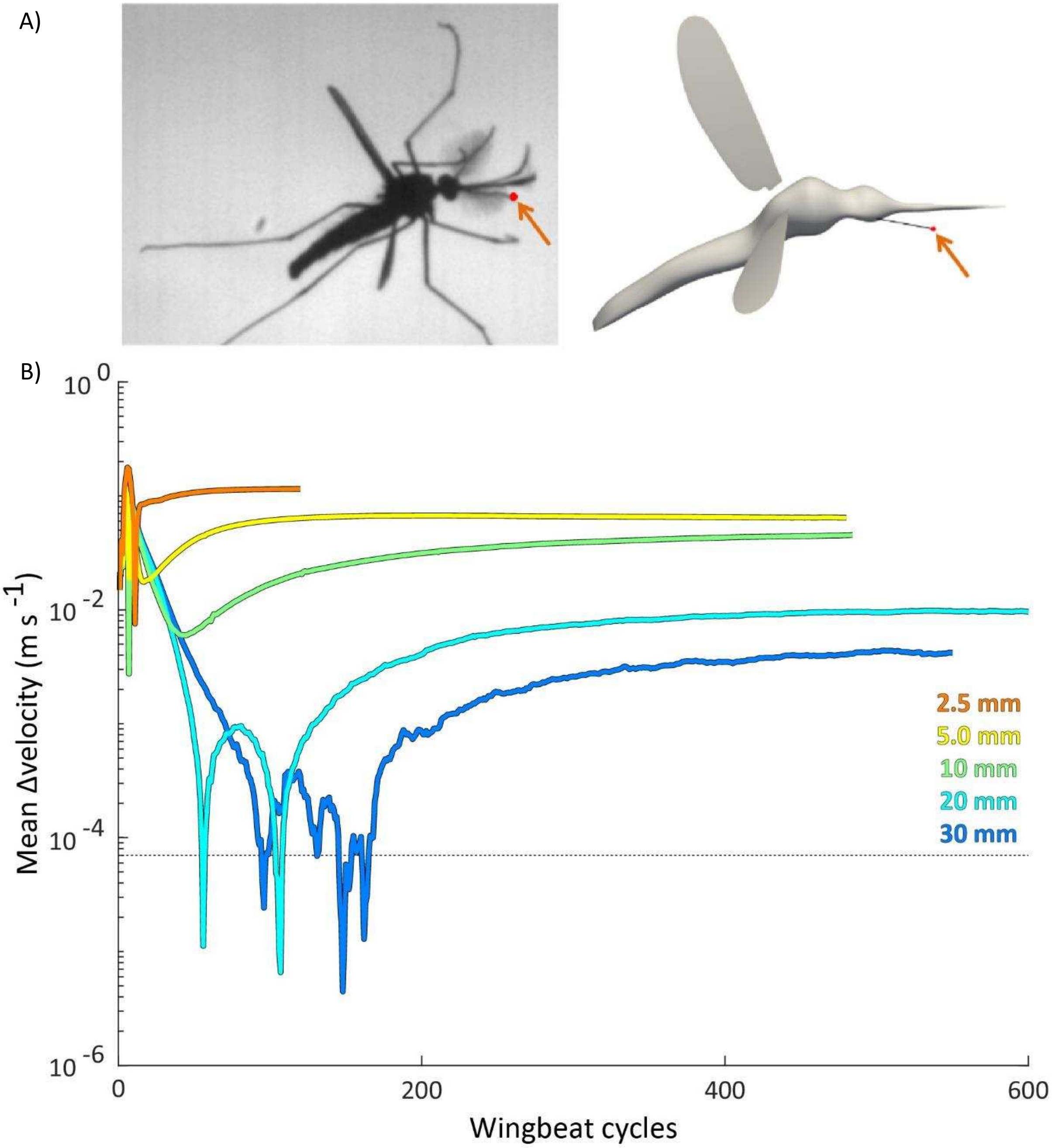

Figure S1: A) location of the antennal tip monitoring location relative to the mosquito body reconstructed from multiple raw data images. B) convergence of the flow field velocity delta with a varying number of wingbeat cycles at selected altitudes.

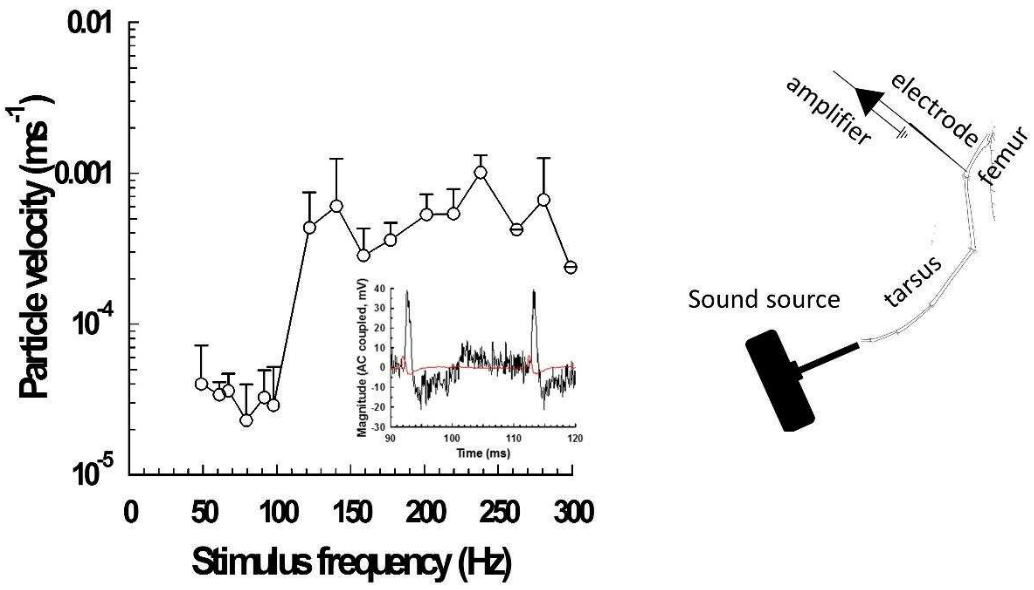

A) B)

Figure S2. Particle velocity threshold (mean + S.D) as a function of stimulus frequency (A) of neural responses recorded from the femurs of the hind legs in response to a vibrating air jet located 2 mm from the claws of the pretarsus with the jet directed parallel to the long axis of the tarsus (B). Inset: Response of a mechanosensory neuron from a male mosquito femur. Intracellular response (black) to the sound stimulus (50 Hz sinusoids, peak particle velocity 5.4×10^{-5} ms^{-1}) and output of particle velocity microphone (red) placed at the stimulus site (pretarsus).

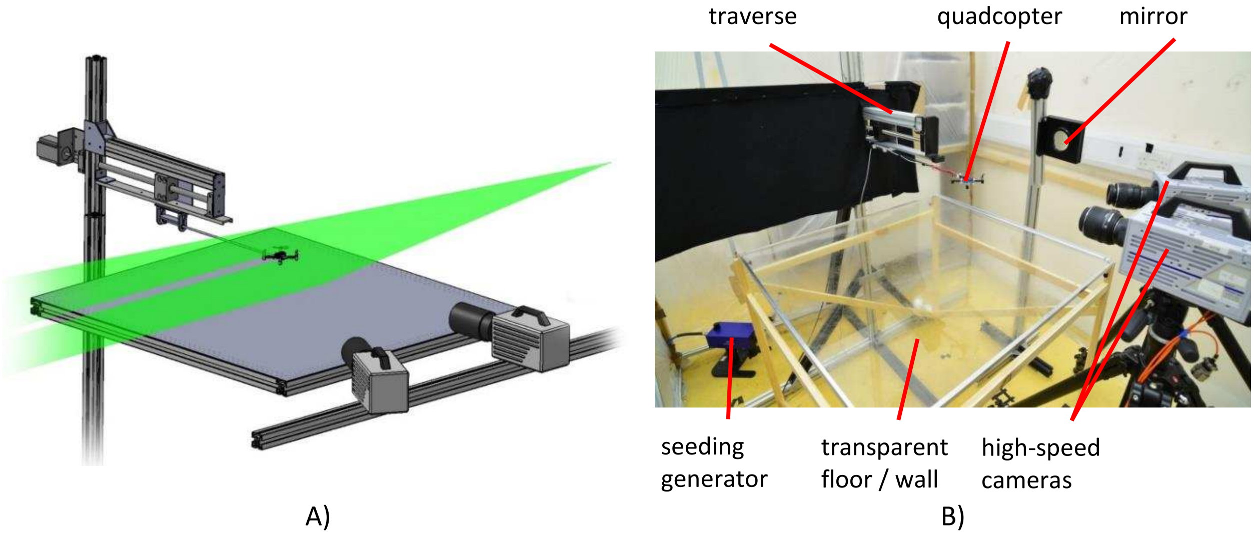

Figure S3. Flow field measurement setup; A) CAD model of apparatus; B) photograph taken in the laboratory.

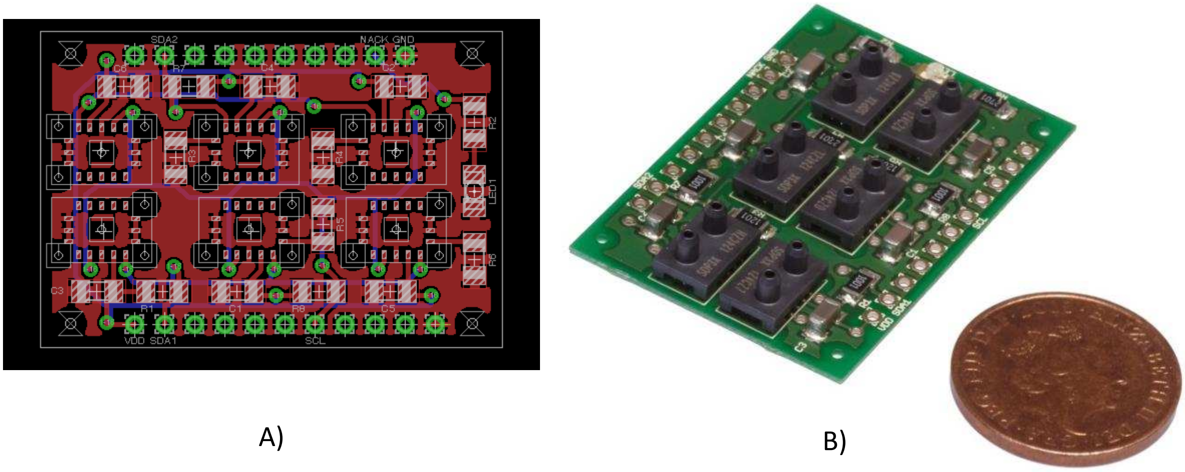

Figure S4. A) pressure sensor array PCB design; B) manufactured PCB fitted with six differential pressure sensors.

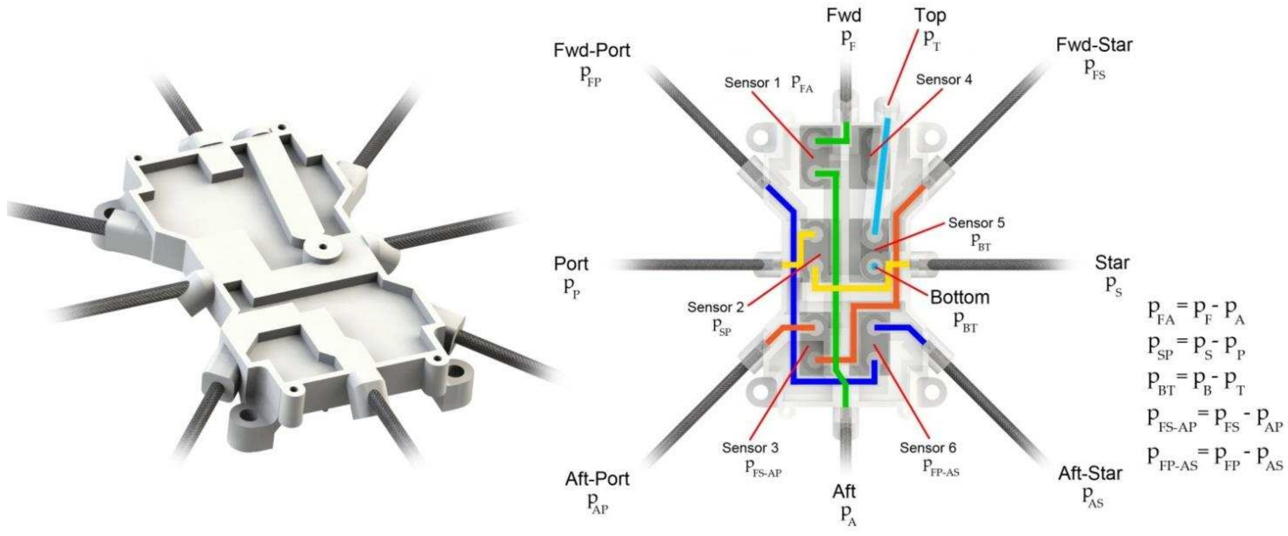

A) B)

Figure S5. Pressure probe attachment; A) CAD model of attachment with extending pressure ports; B) top view of mapping of pressure ports to differential pressure sensors and internal routing tracks (shown in colour) from sensors to ports; Sensor 4 is unused.

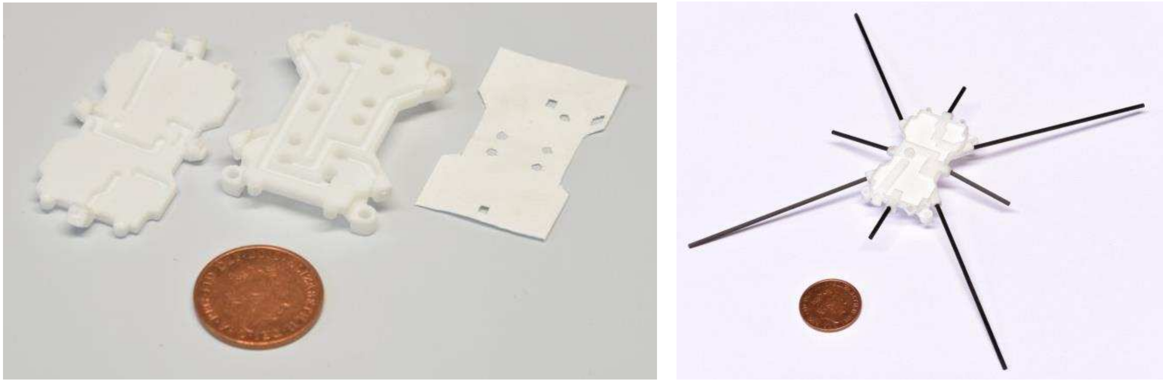

A) B)

Figure S6. A) pressure probe attachment components; B) assembled pressure probe attachment.

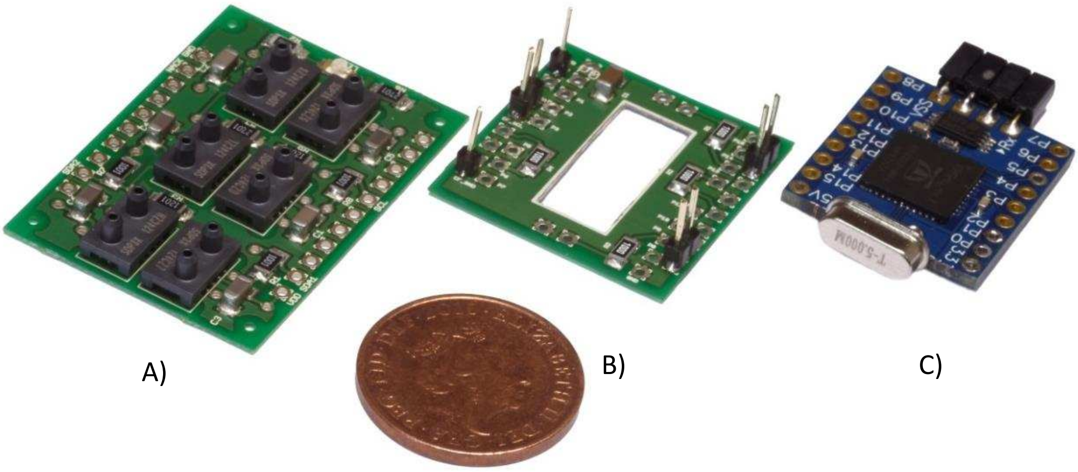

Figure S7. Pressure sensor module components; A) pressure sensor array; B) adapter PCB; C) microcontroller.

Figure S8. Pressure sensor module fitted to the quadcopter underside.

284

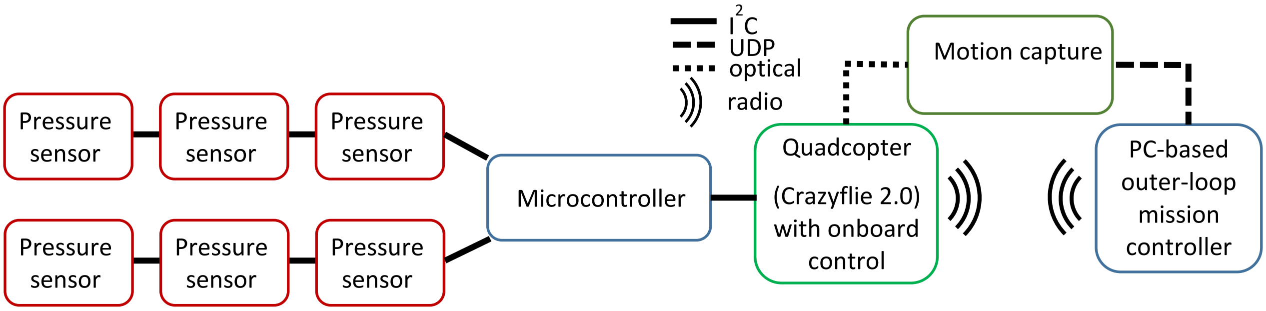

285

286 **Figure S9.** System block diagram of overall platform system architecture, and connection
287 types between elements.

288 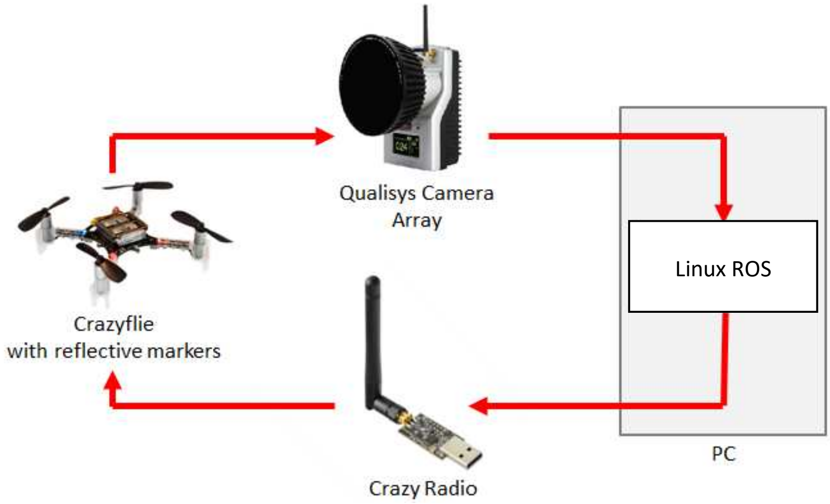

289

290 **Figure S10**: Autonomous flight arena system block diagram.

Proximity condition	**Meaning**
0	No obstacles
1	Near floor proximity
2	Near wall proximity – forward direction
3	Near wall proximity – starboard direction
4	Near wall proximity – aft direction
5	Near wall proximity – port direction

Table S1. Proximity condition definitions.

Component	Mass (g)	Current draw (mA)	Power (mW)
microcontroller	2.5	4	12
pressure sensor array	2.4	19	57
adapter board	1.1	n/a	n/a
pressure probes	3.2	n/a	n/a
Total:	**9.2**	**23**	**69**

294

295 **Table S2.** Mass, current and power breakdown of pressure sensor module components.

Proximity condition	**Meaning**	**$P\Delta_{BT}$ condition**	**$P\Delta_{FA}$ condition**
0	No obstacles	$P\Delta_{BT} < 0.5$	$-0.3 < P\Delta_{FA} < 0.3$
1	Near floor proximity	$P\Delta_{BT} > 0.5$	$-0.3 < P\Delta_{FA} < 0.3$
2	Near wall proximity – forward direction	$P\Delta_{BT} < 0.5$	$P\Delta_{FA} < -0.3$
3	Near wall proximity – starboard direction	n/a	n/a
4	Near wall proximity – aft direction	$P\Delta_{BT} < 0.5$	$P\Delta_{FA} > 0.3$
5	Near wall proximity – port direction	n/a	n/a

Table S3. Proximity conditions with corresponding pressure differential value combinations.

Supplementary Movie 1: Part 1 (0:08). Flow field generated by a flying mosquito visualised using multiple Q iso-surfaces of varying transparencies. Part 2 (0:42). The vortex wake from a mosquito impinging on a ground plane 10 mm below the mosquito body. Part 3 (1:03). Tethered quadcopter fitted with mosquito-inspired, pressure-based surface detection device. Detection of a ground surface is indicated by illumination of four red LEDs. Part 4 (1:28). Detection of a wall is indicated by illumination of a single red LED on the side closest to the obstacle. Part 5 (1:38). Piloted flight of the quadcopter (distance between opposite motor hubs is 95mm) showing repeated detection of a ground surface. Part 6 (1:57). As the quadcopter approaches a vertical wall, the constant blue flight lights reflect off the wall, as well as a single wall-facing red indicator light. Part 7 (2:08). Long exposure photograph of the quadcopter under autonomous control detecting a ground surface in two locations. Mosquito animations slowed down 1000X. Quadcopter videos played back at 1X.